



Post-test analysis of the LAPCAT-II subscale scramjet

Sebastian Karl¹  · Jan Martinez Schramm¹ · Klaus Hannemann¹Received: 12 July 2019 / Revised: 5 February 2020 / Accepted: 9 March 2020 / Published online: 19 March 2020
© The Author(s) 2020

Abstract

A subscale flight experiment configuration propelled by a Mach 8 supersonic combustion ramjet (scramjet) was designed within the framework of the European Commission co-funded Long Term Advanced Propulsion Concepts and Technologies II project. The focus of this design exercise was to verify by ground testing the ability of the proposed scramjet engine to produce adequate thrust for hypersonic level flight. Experiments performed in DLR's High Enthalpy Shock Tunnel Göttingen confirmed precedent CFD predictions of the total thrust and demonstrated the operability of the vehicle. Yet, significant discrepancies between the CFD analyses, which were performed to design the vehicle, and subsequent detailed measurements of the pressure distribution in the combustor were observed and could not be resolved so far. This paper focuses on a further analysis of these residual discrepancies. It was found that the CFD predictions of the combustor pressure distribution are sensitive to the configuration of the intake boundary layer. Particularly, different assumptions for the location of the laminar to turbulent boundary layer transition strongly influence cross-flow structures which develop on the intake and which are able to trigger different combustion modes in the combustor. While the effect on total vehicle performance remains limited, a significant impact on the structure and magnitude of the surface pressure distribution was observed. i.e., the large combustor peak pressures, which occur in the experiment, can be explained by the occurrence of a strong shock train in the vicinity of the combustor wall.

Keywords Scramjet · CFD · Turbulence modeling · Intake flow

Abbreviations

AUSMDV	Advection upstream splitting method, upwind flux splitting scheme
BS	Bow shock (semi-strut H2 injection)
CFD	Computational fluid dynamics
EU-FP7	7th Framework Program of the EU
HEG	High Enthalpy Shock Tunnel Göttingen
LAPCAT	Long Term Advanced Propulsion Concepts and Technologies
MR2	Large-scale Mach 8 cruise configuration in LAPCAT
MUSCL	Monotonic Upwind Scheme for Conservation Laws
RSM	Reynolds stress model (menter)
RBS	Reflected bow shock
RTS	Reflected terminal shock
SA	Spalart–Allmaras turbulence model

SSFE	Small-scale flight experiment
TAU	DLR Navier–Stokes flow solver
TS	Terminal shock
TSP	Temperature-sensitive paint
p	Pressure
P_0	Total pressure
q	Surface heat flux
u	Flow velocity

1 Introduction

The European Commission co-funded research project LAPCAT-II [1] explored technological fundamentals of hypersonic air transport. It was found that scramjet propulsion systems appear to be the most practical option to ensure long-range cruise at flight regimes beyond a Mach number of approximately six. Nevertheless, neither the present technological state-of-the-art nor the empirical experience with these engines allows conclusions about their practical applicability for large-scale and long-range vehicles.

✉ Sebastian Karl
Sebastian.Karl@dlr.de

¹ DLR Institute of Aerodynamics and Flow Technology,
Bunsenstr. 10, 37083 Goettingen, Germany

Substantial further development, testing and qualification are still required to prepare potential future applications.

As a part of this effort, a small-scale flight experiment configuration (SSFE) was derived from the LAPCAT MR2 full-scale vehicle concept for testing in high-enthalpy facilities at DLR and ONERA at flight Mach numbers of about $M=8$. The design of a small engine is particularly difficult. This is due to the unfavorable ratio of wetted surface to volume and the relatively long combustor needed for complete fuel consumption. To compensate for these adverse effects, the SSFE scramjet operates near an equivalence ratio of one and fuel mixing was carefully optimized by a two-stage multi-strut injection concept.

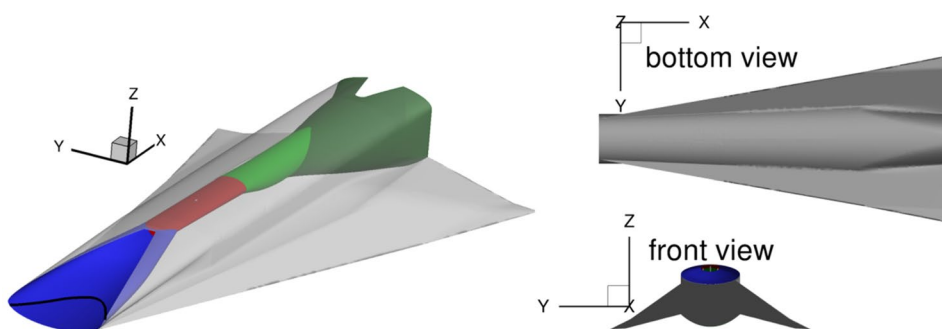
The ground-based testing in DLR's HEG facility [2] confirmed the operability of the vehicle. Good agreement of the general performance characteristics (thrust at different angles of attack and equivalence ratios) between the CFD-based design and the experiments was achieved. However, the experiments also revealed consistent and significant deficiencies of the CFD results regarding the pressure distribution inside the combustor (see Sect. 3). Further analyses of the intake flow [3] showed a strong dependency of the combustor inflow conditions on the boundary layer transition characteristics on the intake. This leads to the hypothesis that the boundary layer properties on the intake can have a substantial impact on the flow structure inside the combustor. The results of detailed heat flux measurements using temperature-sensitive paint [4] which recently became available allow for the first time to prescribe a realistic boundary layer transition behavior to the CFD analyses. This paper investigates the effect of intake boundary layer transition on the combustor operation and discusses the resulting differences with respect to the original vehicle design which was based on the assumption of turbulent boundary layers on the entire intake surface. CFD predictions of the detailed flow properties inside the combustion chamber are assessed based on available high-resolution pressure measurements in Sect. 5. Main characteristics of the combustion process and the flow structure inside the combustor are postulated based on a combination of CFD results and available experimental data.

2 SSFE vehicle layout

The basic layout of the 1.5-m-long hydrogen-fueled vehicle is shown in Fig. 1. The design was driven by the optimal integration of a high-performance propulsion unit within an aerodynamically efficient wave rider design, while guaranteeing sufficient volume for tankage, payload and other subsystems [5]. The optimization of the aerodynamic shape, the propulsion system, the injection concept and initial performance predictions were entirely performed by means of CFD analyses [6].

The inward turning intake was designed based on a modified Busemann template flow field using a 3D stream tracing method. This template flow field consists of a 5° internal conical deflection followed by an isentropic axisymmetric internal compression and a conical terminal shock which redirects the compressed flow in free stream direction [3]. The intake has an elliptical capture area in the yz -plane with a ratio of major to minor axes of three and an overall contraction ratio of about nine. An insert with an elliptical shape in the xy -plane, indicated by the black line on the left part of Fig. 1, was added in front of the streamline traced intake surface to enable smooth integration with the aerodynamic waverider design of the vehicle on the windward side (Fig. 1 (bottom view)). The shape of the upstream part of the waverider windward side dictates the upstream boundary of this insert. The intake feeds an elliptical combustor in which a two-stage multi-strut injector system was installed. The elliptical shape of the internal combustor flow path provides an optimum compromise between wetted area and efficient fuel penetration and mixing. The nozzle was laid out in two sections. The first nozzle section (upstream, light green) has an area ratio of three and blends the elliptical combustor cross section into a circular shape. During ramjet mode, this nozzle is used as an additional combustor and operates in thermally choked mode. The second nozzle section (downstream, dark green) was stream traced from an axisymmetric isentropic expansion and truncated to a suitable length, resulting in an expansion ratio of about ten.

Fig. 1 Schematic of the small-scale scramjet flight configuration under investigation. Blue: intake, red: combustion chamber, green: thrust nozzle, gray translucent: waverider



One of the main challenges of the combustor design was to control the boundary layer separation due to adverse pressure gradients in the vicinity of the combustor entrance. The vehicle does not include boundary layer control devices or bleeds. Thus, the boundary layer entering the combustor is already affected by the strong compression on the intake and is therefore sensitive to separation. To remedy this issue, a diverging combustor geometry and controlled and distributed heat release with a staged injection scheme were foreseen in the design. A combination of an upstream injection stage consisting of two semi-struts and a downstream stage with a central full strut was found to provide the best configuration concerning combustion efficiency, flame anchoring and separation control [6]. The resulting combustor layout is shown in Fig. 2. The distribution of the injected hydrogen at design conditions is indicated by the isosurfaces of 5% mass fraction. The two semi-struts inject about 65% of the gaseous hydrogen fuel through a Mach 2 nozzle normal to the main flow direction. The full strut injects the remaining fuel through 4 Mach 2 nozzles at an angle of 15° with respect to the main flow direction. The hydrogen injected by the semi-struts covers the outboard regions, whereas the full strut distributes fuel into the central part of the combustor. This arrangement also minimizes critical boundary layer disturbances in the upstream central part of the combustor wall which is most sensitive to flow separation.

3 Previous observations

Comprehensive ground-based testing in the HEG facility of DLR confirmed the CFD predictions concerning the net thrust and the general operability of the small-scale vehicle [2]. The free stream conditions of the experiments are summarized in Table 1 and correspond to a flight velocity of Mach 7.4 at an altitude of 27 km. The test time in the HEG shock tunnel was about 3 ms, and the total pressure and enthalpy at the present flow conditions amount to 17.73 MPa and 3.24 MJ/kg, respectively. The ground tests were complemented by detailed CFD analyses of the wind tunnel flow, and good agreement between experimental

Table 1 Free stream conditions

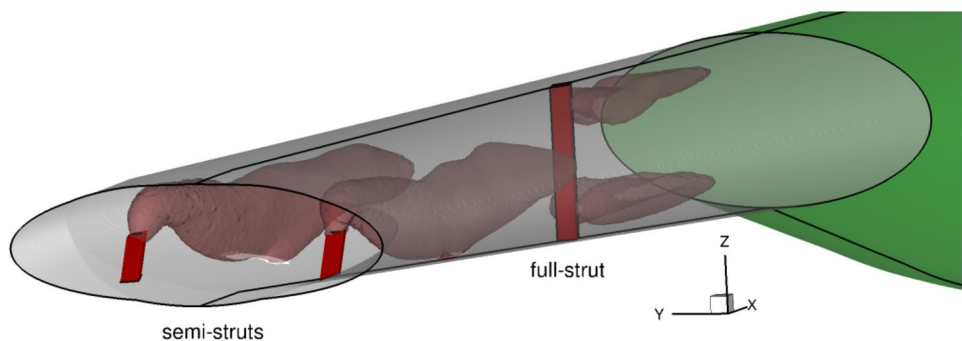
Mach number	7.355	
Static pressure	2060	Pa
Static temperature	263	K
Density	0.02717	kg/m ³
Flow velocity	2396	m/s
Unit Reynolds number	3.8E6	1/m
Angle of attack	-2	°
Total pressure	17.73	MPa

and numerical predictions of the global performance characteristics was achieved.

Besides the successful demonstration of the operability of the vehicle, the wind tunnel tests revealed consistent and significant deficiencies of the CFD predictions of the pressure distribution inside the combustor. A comparison of surface pressure distributions between the CFD design case and the available experimental results is shown in Fig. 3. The results correspond to an angle of attack of -2° and an equivalence ratio of one. The CFD design was based on the assumption of fully turbulent flow (no boundary layer transition), and the Spalart–Allmaras turbulence model was applied.

The location of the surface pressure measurements is indicated by the color of the symbols and the schematic in the figure. Red symbols correspond to the centerline on the intake and thrust nozzle, and black symbols correspond to the combustor side wall. Due to design constraints of the wind tunnel model, no experimental pressure data are available at other locations (e.g., combustor centerline). Because the intake pressure distribution is not affected by the fuel-on operation of the combustor, only side wall pressures are shown for the fuel-on case for clarity (right subfigure). The axial location of the intake leading edge, the combustor entrance, the semi-strut injection ports, the full-strut injection ports and the thrust nozzle entrance are at $x=0, 440, 463, 610$ and 763 mm, respectively. The pressure scales of the fuel-off and fuel-on parts in Fig. 3 are different to clearly highlight the differences in the fuel-off case.

Fig. 2 Combustor layout with injection scheme. Injectors are shown in red, and the computed hydrogen distribution is indicated by the brown isosurfaces of 5% mass fraction



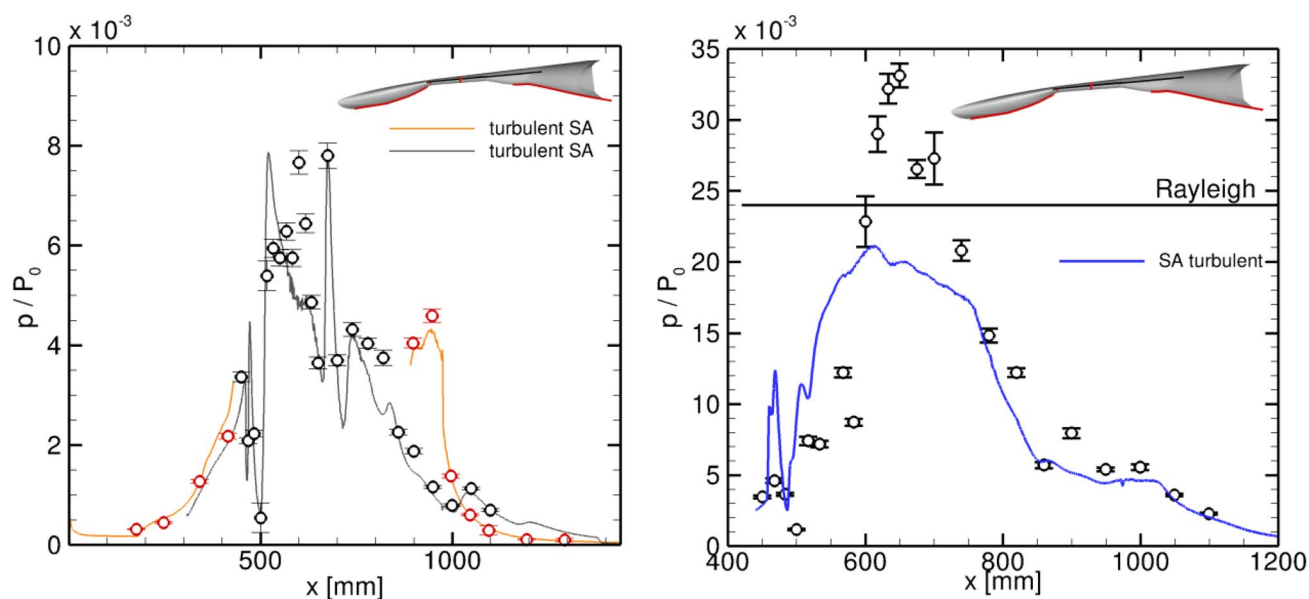


Fig. 3 Fuel-off (left) and fuel-on (right) surface pressure distributions of the design case compared to experimental data; data are normalized by the free stream total pressure, P_0

Large differences between CFD prediction and experimental measurements of the surface pressure distribution on the combustor side wall occur for the fuel-on case. The strong experimental peak at an axial coordinate of 650 mm in Fig. 3 (right) is not reproduced by the numerical analyses of [2]. The location of this peak correlates with the position of the second injector stage. The level of the experimental peak pressure in the combustor exceeds by far the maximum theoretical pressure rise due to hydrogen combustion. This theoretical maximum is indicated by the Rayleigh line in the right part of Fig. 3 (p/P_0 of about 24×10^{-3}). It was evaluated using conservation of total mass, momentum and energy in a diverging duct with heat addition (Rayleigh flow). The assumed heat addition corresponds to complete fuel consumption at an equivalence ratio of one. The equivalent 1D flow properties before heat addition are computed from the CFD solution at the combustor entrance by stream-thrust averaging. The experimental exceedance of the Rayleigh pressure indicates the presence of a strong shock system which was absent in the initial CFD results.

Additional CFD investigations of the isolated intake flow [3] revealed a strong dependence of the flow structure at the combustor entrance on the assumption of the boundary layer transition location on the intake surface in the fuel-off case (corresponding results of the present investigation in Fig. 6). This unexpectedly large effect is due to the accumulation of low-momentum flow along the center plane of the intake driven by cross-flow effects. This cross-flow strongly depends on the local boundary layer thickness which is affected by the transition location. The main objective of the

present investigation was to quantify the effect of the transition location on the flow structure in the combustor and to identify the impact on the CFD prediction of the combustor surface pressure distribution.

4 Numerical model used for the present investigations

All numerical simulations in the present study were performed with the hybrid structured–unstructured DLR Navier–Stokes solver TAU [7]. The TAU code is a second-order finite-volume flow solver for the Euler and Navier–Stokes equations in their integral forms, using eddy viscosity, Reynolds stress or detached and large eddy simulation for turbulence modeling.

For the present investigation, we employed the Spalart–Allmaras one-equation eddy viscosity model [8] and the Wilcox stress-omega Reynolds stress model [9] with a correction to avoid unphysical turbulent production across strong compression shocks [10]. The choice of turbulence models was motivated by the reproduction of the numerical setup used for the vehicle design and the previous test analysis (Spalart–Allmaras) and by the application of a more advanced model (Reynolds stress 7-equation).

The AUSMDV flux-vector splitting scheme was applied together with MUSCL gradient reconstruction to achieve second-order spatial accuracy. Hydrogen combustion was modeled with a finite-rate chemistry approach. The fluid is considered to be a reacting mixture of thermally

perfect gases, with a transport equation solved for each of the individual species. The chemical source terms in this set of transport equations are computed from the law of mass action by summation over all participating reactions. The forward reaction rate is computed using the modified Arrhenius law, and the backward rate is obtained from the equilibrium constant, which is derived directly from the partition functions of the participating species. A modified Jachimowski reaction mechanism [11] for hydrogen–air mixtures was applied for this investigation. This mechanism includes both hydrogen peroxide (H_2O_2) and the perhydroxyl radical (HO_2) and has been shown to be applicable over a wide range of pressures, densities and equivalence ratios. Laminar reaction rates were used, and no specific model for the influence of turbulent fluctuations on the chemical production rates was employed.

The accuracy of the present numerical approach was validated and assessed based on canonical test cases and the HyShot scramjet configuration [12–14].

The free stream conditions are summarized in Table 1 and are representative for the SSFE ground tests in the HEG shock tunnel of the German Aerospace Center, DLR [2]. They correspond to a flight altitude of approximately 27 km.

During ground testing in short-duration facilities the wall temperature remains approximately constant. The test time in HEG was about 3 ms. Hence, the wall temperature is fixed to 300 K for the viscous computations. The computational domain comprises a half model of the vehicle (Fig. 1). The flow inside the hydrogen feeding system was computed separately, and the outflow profiles of the supersonic injection nozzles were prescribed as a Dirichlet condition on the strut surfaces. The unstructured computational grids consist of about 19×10^6 points/volumes for the computational case using the experimental transition line and RSM turbulence model and of about 7.4×10^6 points for all other cases. Boundary layers are discretized with prismatic layers employing a dimensionless wall spacing of $y^+ = O(1)$. The grid convergence of the present computational setup for external and intake flows was demonstrated in [3]. The external and combustor flows were treated in segregated manner to reduce computational cost. The presence of combustion does not have an upstream influence on the intake flow. Hence, the combustion chamber and thrust nozzle (red and green regions in Fig. 1) were treated in a separate computational zone. The inflow conditions were prescribed as a Dirichlet condition (specification of the complete flow state, i.e., velocities, partial species densities and pressure) from a nose-to-tail computation of a complete vehicle. The combustor outflow was then prescribed as a Dirichlet condition in the back to the nose-to-tail grid.

5 Results

5.1 Intake flow

The results of recent measurements of the heat flux distribution on the complete intake surface by temperature-sensitive paint (TSP) [4] were used to prescribe a realistic location of the laminar to turbulent boundary layer transition line as an input for CFD investigations. The error of the TSP data is below 0.035% for the measured temperature [15] which results in an estimated error for the surface heat flux of less than 8%. A resulting numerical heat flux distribution (RSM case) is shown in Fig. 4 together with an indication of the assumed transition line. The figure shows a top view of the front section of the complete vehicle (see Fig. 1, view in negative z -direction). For clarity, heat flux contours are only shown on the intake surface (blue surface in Fig. 1). The assumed boundary layer transition line is shown on all external and internal surfaces which are visible in the 3D top view.

A quantitative comparison of numerical and experimental TSP heat flux profiles along three cuts at 50-, 200- and 350-mm downstream of the leading edge is shown in Fig. 5. The transition line from Fig. 4 (bottom) was used in the turbulent computations; hence, the state of the intake boundary layer in the cuts upstream of 200 mm is always laminar. The agreement in the laminar zone (cuts at 50 and 200 mm) is very good. Minor differences between the CFD curves are related to the application of different grid densities. The cut through the turbulent zone at 350 mm (see also Fig. 4) shows that the Spalart–Allmaras (SA) model over-predicts the experimental heat flux level by about 40%. Improved agreement is achieved when the shock-corrected Reynolds stress model (RSM) is applied.

The flow properties at the combustor entrance show a significant dependency on the boundary layer properties of

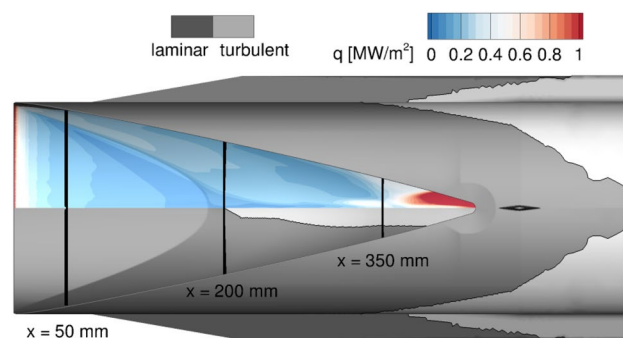


Fig. 4 CFD surface heat flux distribution on the intake surface (top) and locus of the transition line (bottom), light gray, downstream of $x=200$ mm: turbulent regions, dark gray: laminar regions, black lines: locus of the cuts in Fig. 5

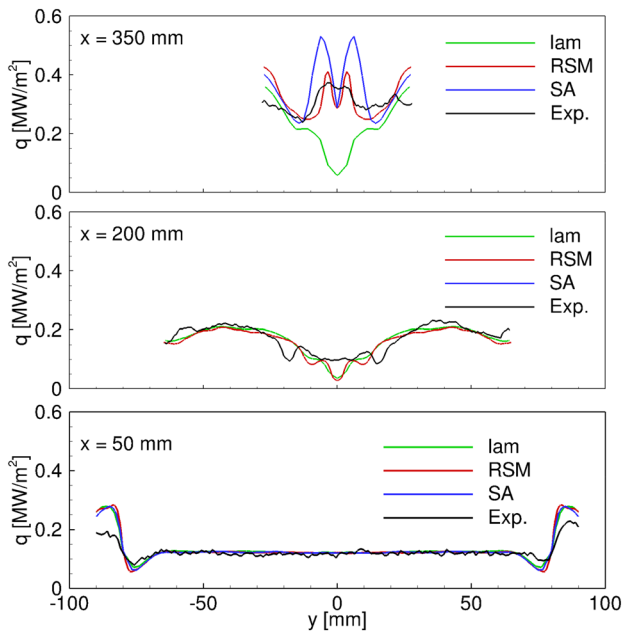


Fig. 5 Heat flux distribution along axial cuts as indicated in Fig. 4; laminar solution (lam) included for reference; experimental values are TSP measurements

the intake. This is related to the development of a pocket of decelerated fluid along the symmetry plane of the intake. Near the combustor entrance, this low-momentum pocket covers about 20% of the cross section of the internal flow path. The flow structure is caused by fluid from inside the boundary layer, which is forced to entrain into the bulk flow near the symmetry plane. This entrainment of low-momentum boundary layer fluid is driven by a strong converging cross-flow. This situation is illustrated by the skin friction lines and axial velocity contours in Fig. 6.

The figure shows the front part and intake of the vehicle in a front-top view. The velocity contours are blanked above 2000 m/s to highlight the extents of the boundary layer and low-momentum structures. The left part of Fig. 6 shows skin friction patterns and low-momentum structures resulting from two different turbulence models and boundary layer transition assumptions (RSM transitional and SA turbulent representing the vehicle design case). The difference in boundary layer thickness is small; however, the structure of the near-wall cross-flow and the pockets of decelerated fluid are clearly affected. Yet, streamlines that are off-set by 2 mm from the wall coincide with the Busemann design as shown in the right part of this figure. This confirms that the cross-flow phenomenon is limited to small layer close to the walls.

The cross-flow is initiated by the sweep in the wall geometry located at the intersection of the insert and the stream-traced compression surface (indicated by the dashed blue line in Fig. 6). The skin friction lines turn sharply inward at this location. The driving mechanism is related to the conservation of the tangential velocity at oblique shocks. The shock originating at the intersection of the insert and the inclined compression surface is misaligned in a near-wall region due to the presence of entropy (blunt leading edges) and boundary layers. Here, the local Mach number and shock angle deviate from the inviscid ideal design based on the template flow field resulting in a misalignment of the flow direction downstream of the shock. A detailed analysis of the cross-flow properties and the related driving mechanisms was performed in previous studies [3].

The cases shown in Fig. 6 show a remarkable difference of the flow structures at the combustor entrance (last downstream cut of axial velocities) between the two considered cases.

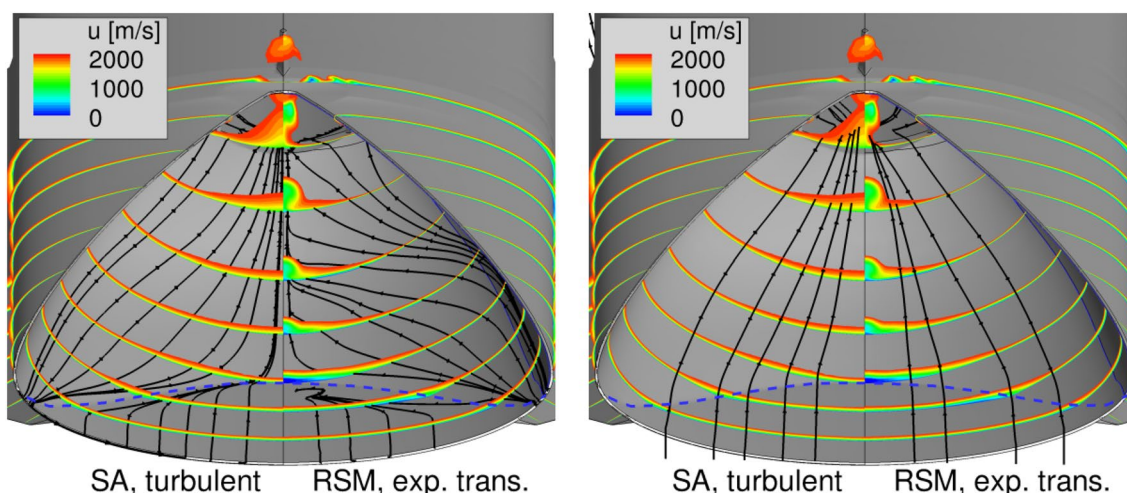


Fig. 6 Skin friction lines at the intake surface (left) and streamlines 2-mm off-set from the wall (right) with contours of axial velocity for different turbulence models and transition locations

5.2 Combustor pressure distributions

Pressure distributions in the combustor and on the intake (fuel-off) and in the combustor (fuel-on) are shown in Figs. 7 and 8. The results in Fig. 7 represent the case of transitional flow and the application of the shock-corrected RSM model. The agreement at fuel-off conditions is slightly improved (reduced over-prediction of surface pressure at $x = 500$ mm), but remarkable differences compared to the numerical setup

which was used during vehicle design (results in Fig. 3, SA model, fully turbulent) are visible for the fuel-on results. A series of strong pressure peaks develops between $x = 550$ and 600 mm. The magnitude of the numerical peak pressures now corresponds to the experimental observations and exceeds the Rayleigh pressure. This indicates the presence of a strong shock structure in the vicinity of the combustor side wall. The surface pressure distribution is characterized by the presence of strong gradients. This is indicated by

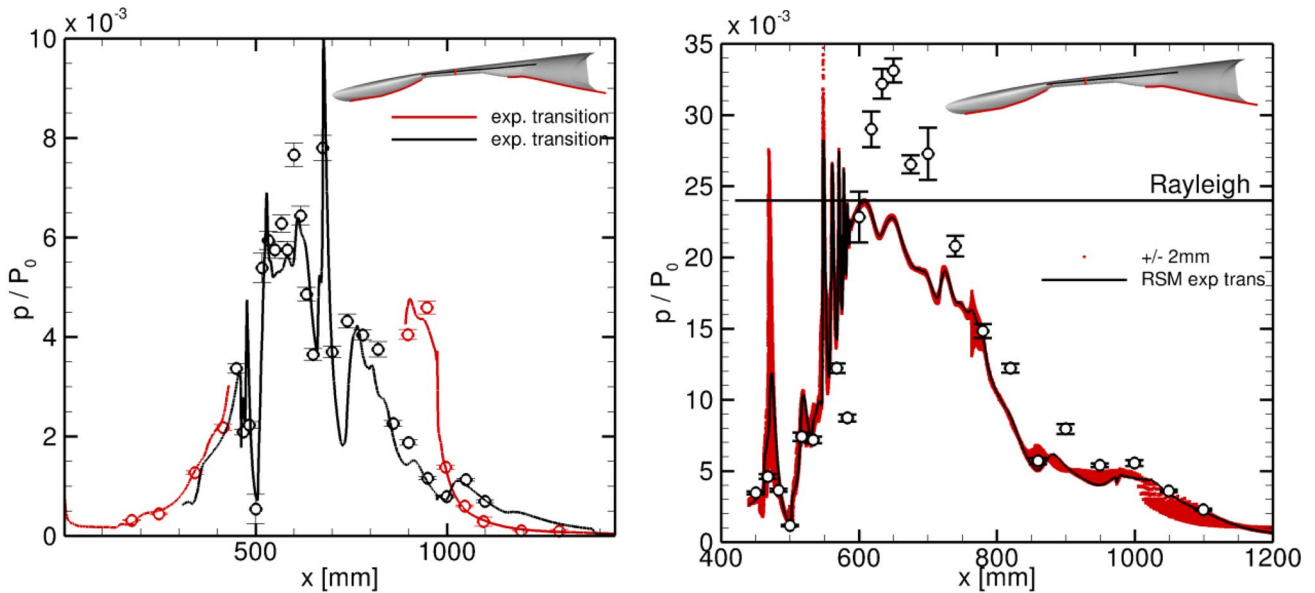


Fig. 7 Surface pressure distribution for the RSM model/transitional flow. Left: centerline (red) and combustor side wall (black); right: combustor side wall (black and red)

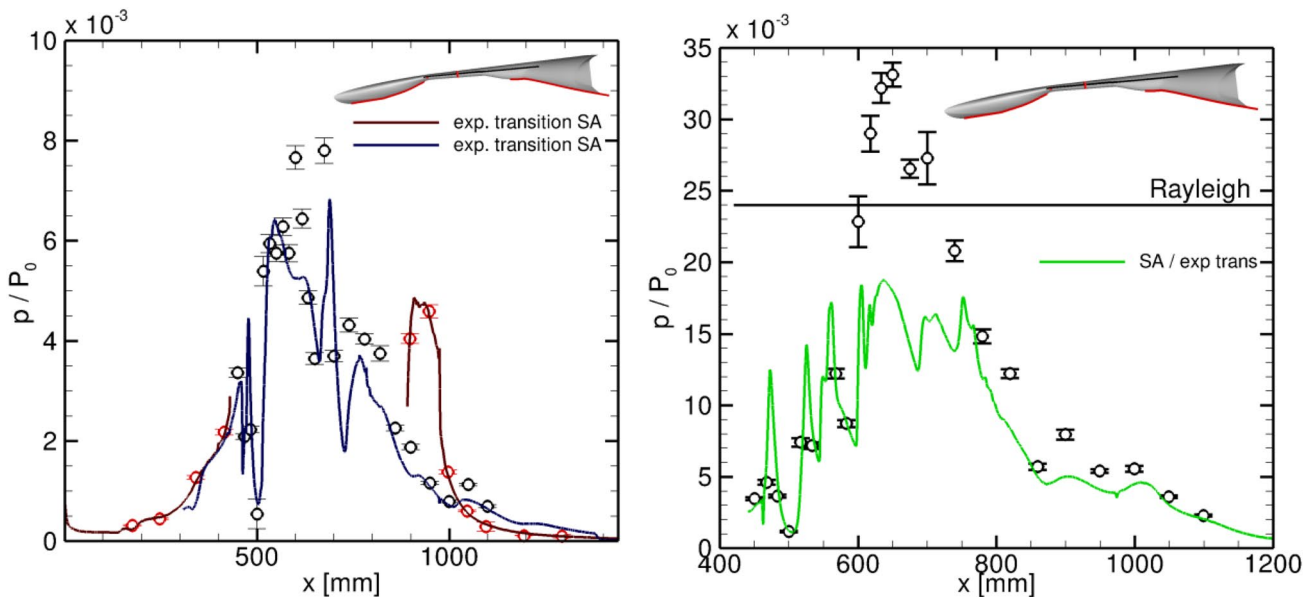


Fig. 8 Surface pressure distribution for the SA model/transitional flow

the red symbols in Fig. 7 which correspond to the pressure range in a region of ± 2 mm around the centerline of the combustor side wall (black line in the combustor schematics and mounting location of the pressure sensors of the wind tunnel model). Nevertheless, the location of the shock train is predicted too far upstream by the numerical simulation.

The pressure distributions in Fig. 8 represent numerical results for the application of the Spalart–Allmaras turbulence model and a reduced reaction mechanism which excludes H_2O_2 and HO_2 [16]. The assumption of the intake boundary layer transition is identical to the results in Fig. 7. The impact on the fuel-off pressure distribution is limited, but, again, significant changes occur in the fuel-on case. The general pressure level between $x=550$ and 750 mm is strongly reduced, and, contrary to the plateau shape of the design case in Fig. 3, pressure peaks are visible which indicated the presence of supersonic flow in the vicinity of the surface.

The fuel-on surface pressures in the nozzle region (downstream section, $x > 750$ mm) are similar for all numerical setups in Figs. 3, 7 and 8. Differences are only visible in the combustor region between $x=550$ and 750 mm. This indicates that, despite remarkable pressure deviations in the combustor region, the vehicle performance (thrust) is not strongly affected by the different modeling assumptions. This is confirmed by the evaluation of the total net thrust from the nose-to-tail computations (difference of the vehicle drag force between fuel-on and fuel-off conditions). This is 536 N for the design case (Spalart–Allmaras turbulent),

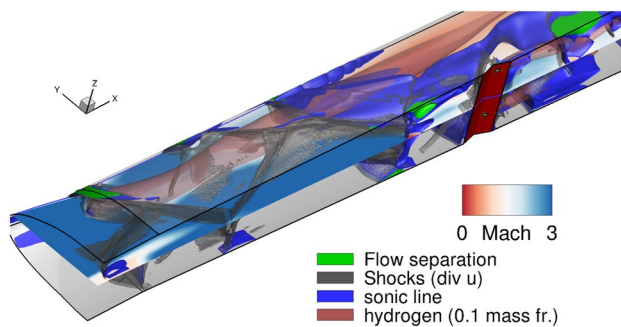
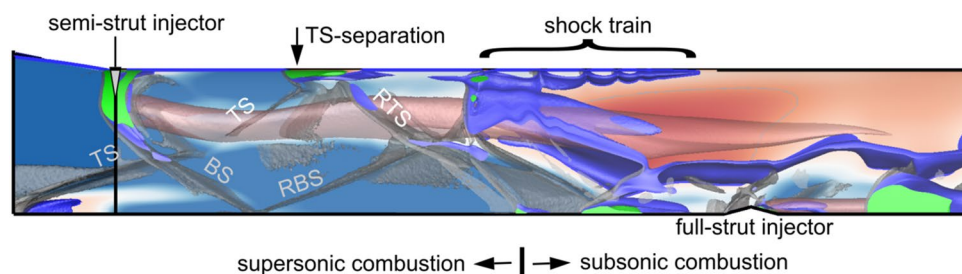


Fig. 9 Flow field structure

Fig. 10 Top view of the flow field structure (*TS* terminal shock, *RTS* reflected terminal shock, *BS* bow shock of the semi-strut hydrogen injection, *RBS* reflected bow shock)



539 N for the transitional RSM case and 529 N for the transitional Spalart–Allmaras case compared to 580 N for the experiment.

5.3 Flow field structure

The strong differences between combustor surface pressure distributions which occur for slightly modified numerical boundary conditions are caused by the occurrence of different flow field structures inside the combustor. Figures 9 (3D view) and 10 (top view) illustrate the flow field in one half of the symmetric combustor for the RSM/transitional computational case for which the best agreement with the experiments was observed (Fig. 7).

The gray isosurfaces of large negative velocity divergence are used to visualize shock structures. Green isosurfaces of negative axial velocity show flow separation zones. The brown surface (H_2 mass fraction of 0.1) indicates the fuel distribution. The sonic line (blue surface) separates supersonic and subsonic flow regions. The Mach number distribution is shown on a cut plane through the centerline of the combustor. The surface pressure results in Figs. 3, 7 and 8 are located at the intersection line of this cut plane and the outboard combustor wall. The combustor entrance is at $x=400$ mm, and the full-strut injector is located at $x=600$ mm.

Different flow structures are labeled in the top view of Fig. 10. The terminal shock (*TS*) entering the combustor is a feature of the Busemann template flow (see Sect. 2) in which the intake design was based on. It is a conical shock wave with the tip anchored at the focal point of the waves emanating from the intake compression surface. It aligns the flow direction after the isentropic intake compression to the axial direction of the combustor. This shock wave is strongly affected by the presence of the low-momentum fluid which enters the combustor due to the presence of the intake cross-flow (see axial velocity contours in Fig. 6). After passing the bow shock caused by the hydrogen injection at the semi-struts (*BS*), the terminal shock is reflected at the combustor wall (*RTS*) and causes flow separation in the vicinity of its impingement point (*TS* separation). A strong shock system is located between a second interaction of the reflected terminal shock (*RTS*) and the reflected bow shock

(RBS) and the semi-strut injector. The major part of the combustor flow is subsonic downstream of this shock system (red Mach number coloring).

The flow structure which produces the prominent pressure peaks as shown in Fig. 7 is a strong shock train which develops in the vicinity of the combustor wall (see Fig. 10). This shock train is initiated at the global normal shock which separates the super- and subsonic combustion zones. The reason of the occurrence of the shock train is the strong gradient of flow properties upstream of the normal shock system. Close to the wall, the flow is not affected by combustion and, therefore, consists of cold air. The combustion zone starts further away from the wall (around the brown H_2 isosurface) and is characterized by hot gas at a reduced Mach number. The Mach number decrease is primarily due to the combustion-driven temperature rise. The pressure rise due to the presence of the normal shock is larger for the cold flow close to the wall than for the hot flow in the combustion zone. The resulting pressure mismatch downstream of the normal shock relaxes in form of a shock train. The physical mechanism is illustrated by means of a model problem in next Sect. 5.4.

5.4 Model problem for the occurrence of the shock train

A generic two-dimensional model problem as illustrated in Fig. 11 is considered to clarify the mechanism of shock train formation. A mixture of air and H_2O at 2000 K (representative for the combustion products in the combustor flame zone) is injected into a slightly diverging channel and forms a normal shock wave to match the specified exit pressure at the outflow boundary. Close to the bottom wall, a thin layer of air at 1500 K is injected. This layer is representative for the flow conditions outside of the combustion zone close to the wall in the upstream part of the SSFE combustor. Both layers share the same inflow velocity and static pressure.

The results in Figs. 11 and 12 show the presence of a shock train and the associated strong pressure oscillations downstream of the initial normal shock wave. Due to the different upstream gas properties, the pressure in the cold

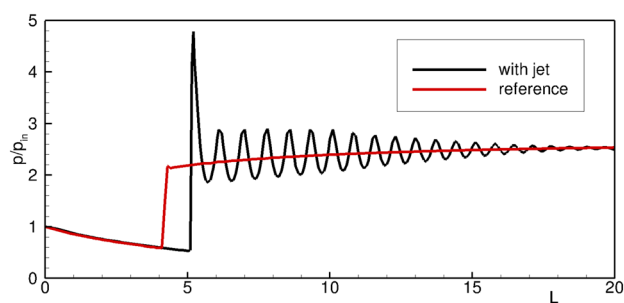


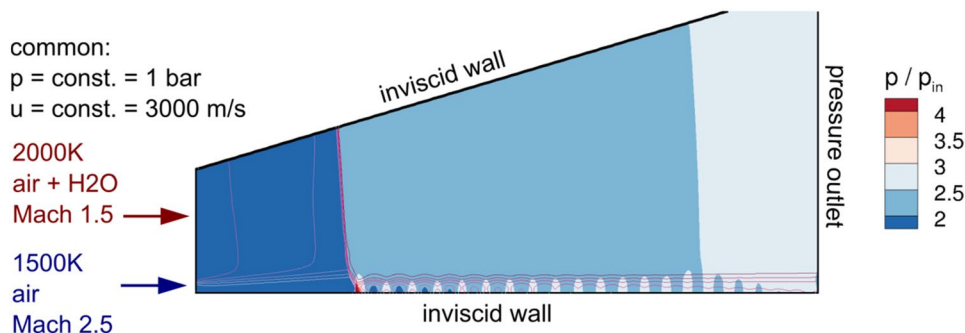
Fig. 12 Surface pressure distribution of the shock train model problem

air jet downstream of the initial shock exceeds the value of the hot air/ H_2O mixture by more than a factor of 2 (see comparison of black and red lines in Fig. 12). The result is the occurrence of a similar flow pattern as for an under-expanded jet in which the static pressure in the cold air jet adapts to the surrounding reference value. This reference pressure in Fig. 12 is resulting from a computation of the pure hot air and H_2O flow at the same boundary conditions. This confirms that the shock train formation in the SSFE combustor is most probably related to the presence of flow property gradients upstream of a strong shock system which results in subsonic flow downstream of it.

5.5 Comparison of flow field structures for the different numerical model setups

The occurrence of the shock train resulting in the reproduction of experimental peak pressures was only achieved for the application of the RSM turbulence model and a realistic assumption for the transition line. Other modeling setups result in different combustion modes (subsonic smooth or supersonic at low pressures) as discussed in Sect. 5.2. The occurrence of these modes is triggered by small changes in the flow topology as illustrated by the schematic flow field structures on the cut plane through the combustor center in Fig. 13. The gray isosurfaces (shocks) and the blue

Fig. 11 Model problem for the occurrence of the shock train (isolines: Mach number)



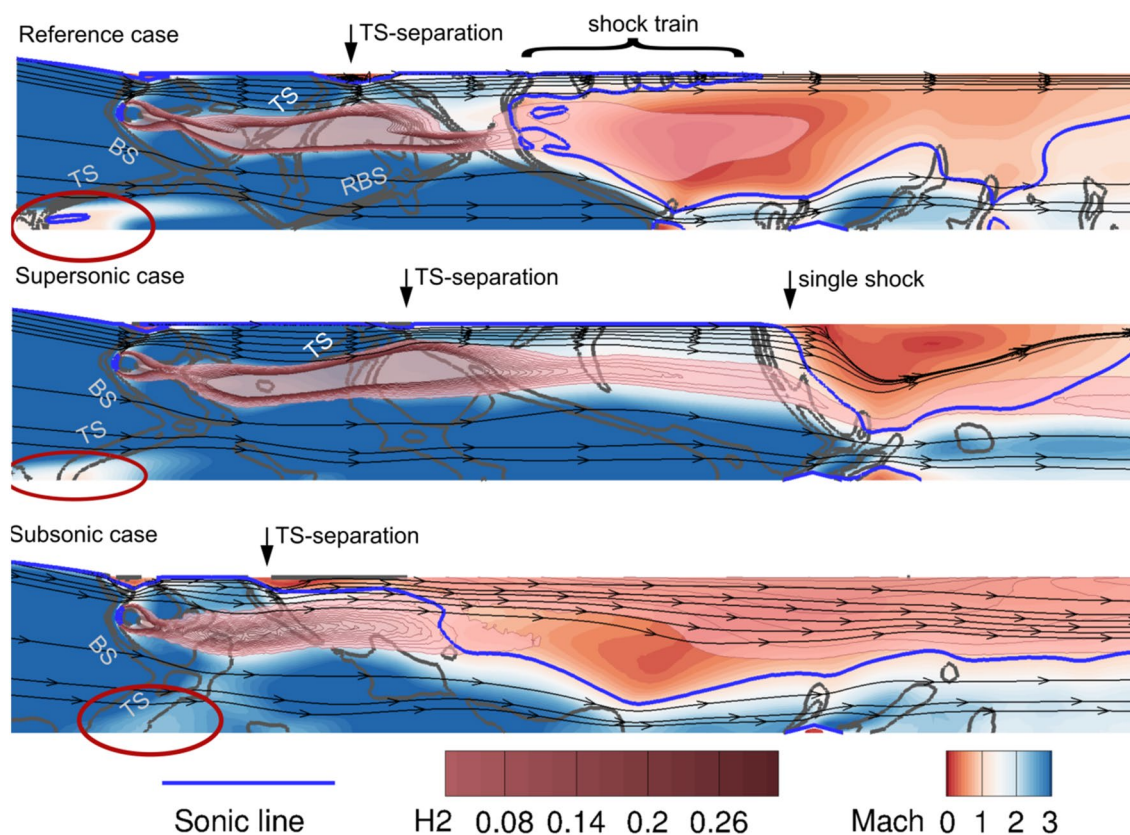


Fig. 13 Flow field structures for the applied numerical modeling setups (reference: RSM/transitional; supersonic: SA/transitional; subsonic: SA/turbulent, red ellipse: footprint of decelerated fluid from intake cross-flow)

isosurface (sonic line) from Figs. 9 and 10 are reproduced as gray and blue lines, respectively.

The top part of the figure represents the reference case (RSM/transitional, details in Fig. 10) for comparison purposes. The main flow features are discussed in Sect. 5.3.

In the supersonic case (Spalart–Allmaras model/transitional), the impingement of the terminal shock at the combustor wall and the associated separation bubble are shifted in downstream direction (TS separation). The separation bubble is smaller, and the effect of this separation, to push the hydrogen jet and the associated combustion zone away from the wall, is less pronounced. The flame zone is closer to the wall and the gradient of cold to hot flow at the beginning of the shock train in the reference case is less pronounced. Here, no shock train is formed and the flow remains supersonic until it reaches a single shock further downstream. This results in a reduced surface pressure at the combustor wall in the supersonic flow region up to $x = 600$ mm (see Fig. 8).

In the subsonic case (Spalart–Allmaras model/turbulent, used during vehicle design), the impingement location of the terminal shock is shifted upstream. The associated separation bubble (TS separation) is larger and entrains hydrogen into the air flow close to the wall. This entrained hydrogen

ignites, and the combustion zone is extended up to the wall. The flow becomes subsonic at this separation-driven combustion zone and remains subsonic in downstream direction. This results in the smooth pressure variation shown in Fig. 3.

For all cases, the angle and configuration of the terminal shock is affected by the pocket of decelerated fluid which enters the combustor. The footprint of this pocket is highlighted by the red ellipses in Fig. 13. This shock configuration and the strength of the associated terminal shock separation (TS) influence the geometrical location of the combustion zone and the associated flow structure and pressure distribution at the combustor wall.

6 Conclusion

The large discrepancy between the observed numerical surface pressure distributions in Figs. 3, 7 and 8 is due to the occurrence of different flow structures close to the combustor side wall. Supersonic flow causes low pressures with visible peaks, and subsonic flow results in a smooth variation of pressure. Only an in-between mode, in which a local shock train occurs, reproduces the experimental peak pressures. The combustion modes are triggered by the

geometrical distribution of the flame zone. This distribution is affected by the configuration of the terminal shock of the intake flow entering the combustor and the strength of a local separation bubble at its impingement point on the combustor side wall. The structure of the terminal shock is altered as it passes through a pocket of decelerated fluid at the combustor entrance. Cross-flow, which occurs close to the intake surface, generates this low-momentum fluid. The structure of the cross-flow pattern is strongly affected by the turbulence model and transition assumption for the intake flow. By this mechanism, the numerical simulation results for the combustor pressure distribution are very sensitive to the modeling of the intake boundary layer.

The combustor pressures which are experimentally observed exceed the Rayleigh pressure and clearly indicate the presence of a strong shock train close to the surface. Present numerical simulations using a realistic assumption for the laminar to turbulent transition on the intake reproduce the peak pressure level. Yet, the location of the peak pressures is predicted too far upstream. Generally, the flow structure in the combustor is characterized by a complex interplay of turbulent flow, shock and expansion waves and combustion. Hence, the application of scale-resolving turbulence models together with improved boundary layer transition prediction in the regions which are not accessible by the experiment (e.g., upper part of the combustor) are likely to lead to improved predictions in the future.

Despite the large discrepancies of surface pressure on the combustor wall, the pressure distributions on the thrust nozzle and the integral vehicle performance are insensitive to the different modeling assumptions used in the present study.

Acknowledgements Open Access funding provided by Projekt DEAL.

Open Access This article is licensed under a Creative Commons Attribution 4.0 International License, which permits use, sharing, adaptation, distribution and reproduction in any medium or format, as long as you give appropriate credit to the original author(s) and the source, provide a link to the Creative Commons licence, and indicate if changes were made. The images or other third party material in this article are included in the article's Creative Commons licence, unless indicated otherwise in a credit line to the material. If material is not included in the article's Creative Commons licence and your intended use is not permitted by statutory regulation or exceeds the permitted use, you will need to obtain permission directly from the copyright holder. To view a copy of this licence, visit <http://creativecommons.org/licenses/by/4.0/>.

References

1. Steelant, J.: Sustained Hypersonic flight in Europe: technology drivers for LAPCAT II. In: 16th AIAA/DLR/DGLR International Space Planes and Hypersonic System Technologies Conference, Bremen, Germany, AIAA 2009-7240 (2009)
2. Hannemann, K., Martinez Schramm, J., Karl, S., Laurence, S. J.: Free flight testing of a scramjet engine in a large scale shock tunnel, AIAA 2015-3608. In: 20th AIAA International Space Planes and Hypersonic Systems and Technologies Conference, Glasgow (2015)
3. Karl, S., Steelant, J.: Crossflow phenomena in streamline-traced hypersonic intakes. *J. Propul. Power* **34**(2), 449–459 (2018)
4. Martinez Schramm, J., Karl, S., Ozawa, H., Hannemann, K.: Heat flux measurements by means of ultra-fast temperature sensitive paints on the intake of the small scale flight configuration of the LAPCAT II vehicle in the high enthalpy shock tunnel Göttingen. In: HiSST: International Conference on High-Speed Vehicle Science Technology, Moscow, Nov. 26–29 (2018)
5. Murray, N., Steelant, J., Mack, A.: conceptual design of a mach 8 hypersonic cruiser with dorsal engine. In: Proceedings of the Sixth European Symposium on Aerothermodynamics for Space Vehicles, ESA SP-659, European Space Agency, ISBN 978-92-9221-223-0 (2009)
6. Langener T, Steelant J., Karl S., Hannemann K.: Layout and design verification of a small scale scramjet combustion chamber. In: Proceedings of the XXI International Symposium on Air Breathing Engines (ISABE 2013), ISABE Paper 2013-1655 (2013)
7. Langer, S., Schwöppe, A., Kroll, N.: The DLR flow solver TAU—status and recent algorithmic developments, AIAA Paper 2014-0080 (2014)
8. Spalart, P.R., Allmaras, S.R.: A one equation turbulence model for aerodynamic flows. *La Recherche Aérospatiale* **1**, 5–21 (1994)
9. Wilcox, D.C.: Turbulence Modeling for CFD. DCW Industries Inc., La Canada (2006)
10. Karl, S., Hickey, J.P., Lacombe, F.: Reynolds stress models for shock: turbulence interaction. In: 31st International Symposium on Shock Waves **1**, 511–517, Springer (2018) <https://doi.org/10.1007/978-3-319-91020-8>
11. Gerlinger, P.: An implicit multigrid method for turbulent combustion. *J. Comput. Phys.* **167**, 247–276 (2001)
12. Karl, S.: numerical investigation of a generic scramjet configuration, Ph.D. Dissertation, Faculty of Mech. Eng., Technical University Dresden (2011) [available online] URL: <http://mbn-resolving.de/urn:nbn:de:bsz:14-qucosa-68695>. Accessed Jan 2017
13. Hannemann, K., Karl, S., Martinez Schramm, J., Steelant, J.: Methodology of a combined ground based testing and numerical modelling analysis of supersonic combustion flow paths. *Shock Waves* **20**(5), 353–366 (2010). <https://doi.org/10.1007/s00193-010-0269-8>
14. Laurence, S.J., Karl, S., Schramm, J.M., Hannemann, K.: Transient fluid-combustion phenomena in a model scramjet. *J. Fluid Mech.* **722**, 85–120 (2013)
15. Martinez Schramm, J., Edzards, F., Hannemann, K.: Calibration of fast-response temperature sensitive paints for their application in hypersonic high enthalpy flows, new results in numerical and experimental fluid mechanics XI, pp. 141–151, Springer (2016)
16. Gaffney, R.L., White, J.A., Girimaji, S.S., Drummond, J.P.: Modeling turbulent chemistry interactions using assumed pdf methods. In: 28th AIAA/SAE/ASME/ASEE Joint Propulsion Conference and Exhibit (1992)

Publisher's Note Springer Nature remains neutral with regard to jurisdictional claims in published maps and institutional affiliations.